RSC Applied Interfaces

ROYAL SOCIETY OF CHEMISTRY

PAPER

View Article Online
View Journal | View Issue

Cite this: *RSC Appl. Interfaces*, 2025, **2**, 1702

Water-soluble fluorine-free poly(ionic liquid) borate binders for Li-ion battery cathodes

Haris Amir, [a] Ana Clara Rolandi, [b] Gabriele Lingua, [b] Maria Forsyth, [cd] Małgorzata Swadźba-Kwaśny, [a] John D. Holbrey, *[a] David Mecerreyes [bd] and Nerea Casado *[bd]

Received 26th May 2025,
Accepted 5th August 2025

DOI: 10.1039/d5lf00155b

rsc.li/RSCApplInter

The development of efficient, eco-friendly lithium-ion battery (LIB) technologies necessitates alternative binder materials to replace conventional polyvinylidene fluoride (PVDF). Five novel water-soluble poly(ionic liquid) (PIL) binders based on poly(diallyldimethylammonium) (PDADMA) with borate counter-anions are presented. The binders—PDADMA–C4B, PDADMA–C3B-A, PDADMA–C3B-B, PDADMA–PyrB, and PDADMA–TriB were synthesised and characterised for thermal stability, electrolyte uptake, adhesion, and electrochemical performance. Among these, PDADMA–C4B demonstrated superior properties, including high thermal stability (>200 °C), significant electrolyte uptake (303%), and low internal resistance, leading to improved cycling performance of LIB. At high C-rates, PDADMA–C4B outperformed PVDF, maintaining structural integrity and higher discharge capacities. Surface analyses confirmed minimal degradation, underscoring the durability of the PDADMA–borate binders. These results highlight PDADMA–C4B as a sustainable, high-performance alternative to fluorinated binders, promoting advancements in LIB technology.

Introduction

The demand for lithium-ion batteries (LIBs) is rapidly increasing due to their widespread use in advanced technologies, such as electric vehicles and renewable energy storage. This surge in demand presents significant challenges for the development of efficient and sustainable battery systems.[1] A typical LIB electrode comprises active materials, conductive additives, and binders, with the binder playing a crucial role in maintaining the structural integrity and performance of the electrode. It ensures cohesion between active materials and conductive additives, good adhesion to the current collector, and effective ionic percolation by providing polymer–electrolyte domains for Li^+ conduction.[2] These factors are essential for the overall performance and longevity of the battery.[3]

Traditionally, polyvinylidene fluoride (PVDF) has been the binder of choice in commercial LIB cathodes due to its excellent chemical and electrochemical resistance, thermal stability, and strong adhesive properties.[4] However, PVDF presents several drawbacks. Its manufacturing process involves the use of toxic solvents like *N*-methyl-2-pyrrolidone (NMP), raising significant environmental and health concerns.[5] Consequently, an expensive solvent recovery system is required for proper disposal of NMP, and temperatures exceeding 100 °C are necessary for the drying step of electrode preparation due to the high boiling point of NMP. Additionally, the presence of fluorine atoms in the polymer poses challenges for LIB recycling. These issues have driven the search for alternative binder materials that can enhance electrochemical performance while supporting a more eco-friendly production process.[6]

As a result, significant research has focused on exploring alternatives to the organic solvent-based processes required with PVDF. One promising solution is the use of solvent-free fabrication techniques such as dry spraying deposition, hot melting, and 3D printing, which eliminate the need for harmful solvents.[7] Alternatively, water-soluble polymers and biopolymers such as carboxymethyl cellulose (CMC), polyacrylic acid (PAA), and alginates have gained attraction as a more environmentally friendly binder option for electrode processing.[8]

Poly(ionic liquids) (PILs) have emerged as promising binders for energy storage applications. These ionic polymers, composed of cationic or anionic species bonded to a polymer backbone, offer a unique combination of

[a] *The QUILL Research Centre, School of Chemistry and Chemical Engineering, Queen's University Belfast, David Keir Building, Stranmillis Road, Belfast BT9 5AG, UK. E-mail: j.holbrey@qub.ac.uk*
[b] *POLYMAT, University of the Basque Country UPV/EHU, Avenida Tolosa 72, 20018 Donostia-San Sebastian, Spain. E-mail: nerea.casado@ehu.eus*
[c] *Institute for Frontier Materials, Deakin University, Geelong, Victoria 3217, Australia*
[d] *Ikerbasque, Basque Foundation for Science, 48009 Bilbao, Spain*

advantageous characteristics: ionic conductivity, flexibility, and wide electrochemical stability windows.[9] The ability to tailor and integrate these properties to meet specific requirements makes PILs a versatile and effective platform for enhancing the efficiency and safety of energy storage devices.[10] Furthermore, the tunable nature of PILs allows for performance optimization across various applications, positioning them as a viable alternative to traditional binders.[11]

Poly(diallyldimethylammonium) (PDADMA)-based PILs are particularly attractive materials for use as potential binders. PDADMA can be modified with various counter-anions, such as $TFSI^-$, FSI^-, and BF_4^-, which enhance its electrochemical performance.[12,13] The incorporation of ionic charges into the polymer structure improves lithium diffusion and long-term stability, making it applicable as a promising binder candidate for use in both anodes and cathodes of LIBs.[14] The solubility of PDADMA PILs can be tuned with the selection of the counter-anion. Recently, water-soluble PDADMA binders were developed with phosphate anions for water processing of NMC cathodes, showing comparable cycling and stability results to PVDF binders.[15]

Here, we explore the incorporation of five new borate anions, including examples we have recently demonstrated as effective in forming room-temperature conductive organic ionic plastic crystals,[16] in PDADMA-based binders and investigate their impact on the electrochemical performance of LIBs. These PDADMA–borate binders are compared with conventional water-soluble binders like Na-CMC and PVDF processed in NMP to assess their viability as environmentally friendly, high-performance alternatives in the next generation of LIBs.[3,17] The primary objective of this work is to evaluate the electrochemical performance of fluorine-free, water-soluble PDADMA-based binders that incorporate borate anions. By synthesising and characterising these PDADMA–borate binders, we aim to demonstrate their potential as sustainable, high-performance alternatives to traditional binders, contributing to the development of more efficient and eco-friendly lithium-ion batteries.[18]

Results and discussion

Preparation and physicochemical characterisation of PDADMA–borates

Five water-soluble poly(ionic liquids) (PILs) bearing different borate anions have been prepared by anion exchange reaction as shown in Fig. 1. Commercially available PDADMACl was first passed through a column with the exchange resin IRN78, to obtain PDADMA–OH. Then PDADMA–OH was mixed with the corresponding acid borate, to obtain the five PDADMA–borate polymers named PDADMA–C4B, PDADMA–C3B-A, PDADMA–C3B-B, PDADMA–PyrB, and PDADMA–TriB. The borates containing N/O–chelating ligands derived from functionalised alkanolamines; $[B(C_4H_9NO)_2]^-$ (C4B), $[B(C_3H_7NO)_2]^-$ (A) (C3B-A), and $[B(C_3H_7NO)_2]^-$ (B) (C3B-B) were synthesised using a modification of the method described by Chiappe *et al.*[19] for

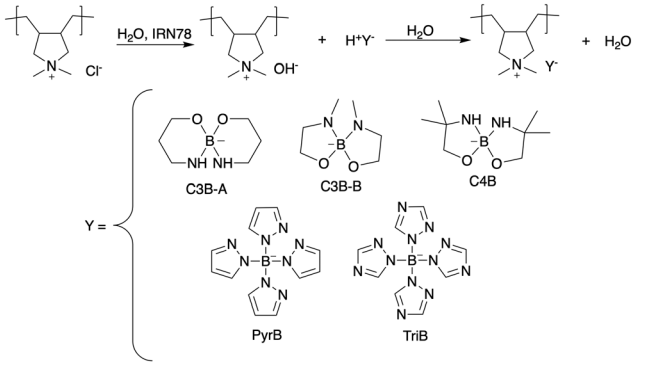

Fig. 1 The reaction scheme for the synthesis of PDADMA–borates poly(ionic liquid)s.

the preparations of O/O-chelated orthoborates. The tetrakis(azolyl)borate anions, $[B(pyrazole)_4]^-$ (PyrB) and $[B(triazole)_4]^-$ (TriB), were synthesised using the method described by Chao *et al.*;[20] the formulas, abbreviations, and structures are shown in Table S1 in the SI. The chemical structure of these PDADMA–borates was confirmed by ^1H, ^{13}C, and ^{11}B NMR spectroscopy, which can be found in the SI (Fig. S1–S28).

Fig. 2(a) shows the ^1H NMR spectrum of PDADMA–C4B. The spectrum includes peak assignments and integrations, indicating a 1 : 1 ratio of cation to anion. This confirms the presence of the PDADMA cation and the $[B(C_4H_9NO)_2]^-$ anion. The overlaid ^{11}B NMR signals of PDADMA–C4B and $H[B(C_4H_9NO)_2]$ (Fig. 2(b)) show the successful anionic exchange of the OH^- with the $[B(C_4H_9NO)_2]^-$ anion, as there is no signal of the parent $H[B(C_4H_9NO)_2]$ present in the PDADMA–C4B. This behaviour was also observed for the other PILs and the NMRs can be observed in Fig. S1–S28.

Comparing the FTIR spectra of PDADMA–C4B with those of PDADMA–Cl (Fig. 2(c)) reveals two new prominent bands. The band at 1045 cm^{-1} is assigned to the B–O stretching mode, while the band at 1317 cm^{-1} corresponds to B–N stretching vibrations. These values align with the characteristic vibration modes of the boron–oxygen and boron–nitrogen bonds in borate compounds[19,21] confirming the successful formation of the PDADMA–borate PILs. All PDADMA–borates reported in this study (Fig. S29 in SI) show characteristic peaks of the B–N stretching band (1317 cm^{-1}), and the three PDADMA–borates with N/O-chelated borate anions (C3B-A, C3B-B and C4B) also exhibit a distinctive stretch peak of B–O (1045 cm^{-1}).

Thermal behaviour

The thermal stability of PDADMA–borates was evaluated by thermogravimetric analysis (TGA), as shown in Fig. 3(a) (i). All PDADMA–borate PILs are essentially stable to at least 170–200 °C (2% mass loss): C4B exhibits the lowest onset at 170 °C, C3B-A 180 °C, PyrB 185 °C, C3B-B 200 °C and TriB the highest at 240 °C (Table S2). A minor mass loss (<1%) below 100 °C is attributed to residual moisture, beyond 200 °C multi-

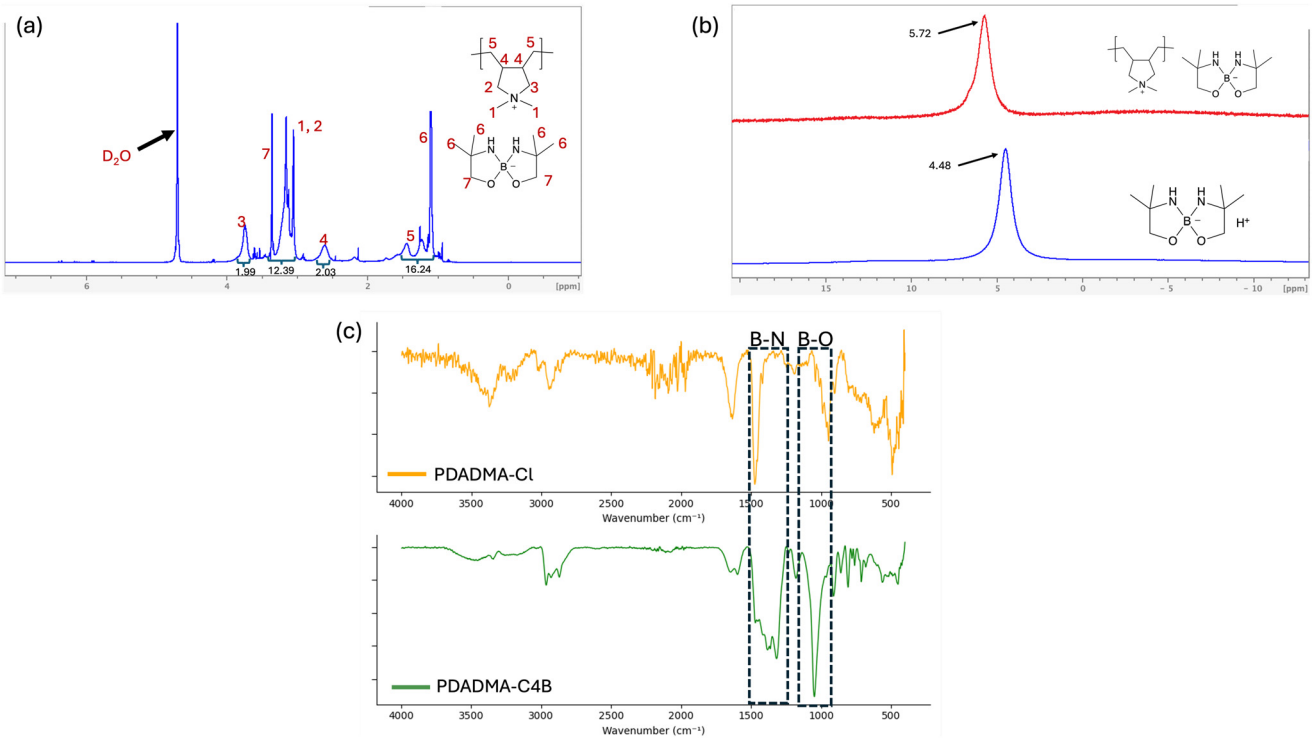

Fig. 2 (a) ^{1}H NMR spectrum of PDADMA–C4B in D_2O, (b) ^{11}B NMR signals from PDADMA–C4B (top) and H[B($C_4H_9NO)_2$] (bottom), and (c) FTIR spectra of PDADMA–Cl and PDADMA–C4B.

step degradation is observed. As a typical example, PDADMA–C4B begins to decompose around 200 °C, undergoing a rapid 40 wt% loss. This is followed by a second stage of mass loss, accounting for another 40 wt%, between 300 °C and 500 °C. Beyond this, no further mass loss is observed. The multistep degradation behaviour is probably attributed to the contributions of the anion and the polymer backbone.

The thermal stability of the PDADMA–borates, ranked by their onset decomposition temperatures, is as follows: PDADMA–C3B-B > PDADMA–C4B > PDADMA–C3B-A > PDADMA–PyrB > PDADMA–TriB. Among these, PDADMA–C3B-B shows the highest onset temperature (290 °C), indicating the greatest thermal stability, while PDADMA–TriB has the lowest onset temperature (200 °C), signifying the least stability. For comparison, the degradation temperatures of PVDF and Na-CMC are 240 °C and 150 °C, respectively.[22]

The phase behavior of these compounds was investigated using differential scanning calorimetry (DSC) (see Fig. S30 in the SI). However, no slope variations indicating glass transition (T_g) or other phase transitions (melting or crystallization) were observed within the temperature range of −85 to 160 °C. Despite this, it can be concluded that all the PDADMA–borates discussed in this study are suitable for the temperature range required for LIB electrode processing.

Electrolyte uptake

Electrolyte uptake is crucial for binders because it affects the ionic conductivity and overall battery performance. High electrolyte uptake enhances the interface between the binder and active materials, promoting efficient ion transport and improving cell efficiency and stability during charge–discharge cycles, ensuring long-term reliability of the battery.[23]

A swelling test of the binders was conducted to investigate their suitability and stability in electrolyte solutions, and the electrolyte uptake was calculated using eqn (1). A larger electrolyte uptake typically correlates with more effective transport of ions through the electrode by creating pathways for them to diffuse.[24] However, excessive swelling can compromise mechanical integrity and lead to electrode cracking or delamination. In this study, no visible degradation or binder delamination was observed even for the highest-uptake binder (PDADMA–C4B), indicating that the interpenetrating polymer–electrolyte network remained mechanically robust. After five days' immersion, excess electrolyte was gently removed by patting the films with tissue before weighing. The mass increase, corresponding to electrolyte uptake into the PILs, is shown in Fig. 3(b), with uptake following the order from highest to lowest: PDADMA–C4B (303%) > PDADMA–C3B-A (228%) > PDADMA–TriB (122%) > PDADMA–PyrB (124%) > PDADMA–C3B-B (93%). The polar N–H functionalities in the borate anions of PDADMA–C4B and PDADMA–C3B-A likely contribute to their higher affinity for electrolyte solvents, resulting in the observed greater uptake. In contrast, commonly used binders such as PVDF and Na-CMC exhibit much lower mass increases upon immersion, with reported values of 2% and

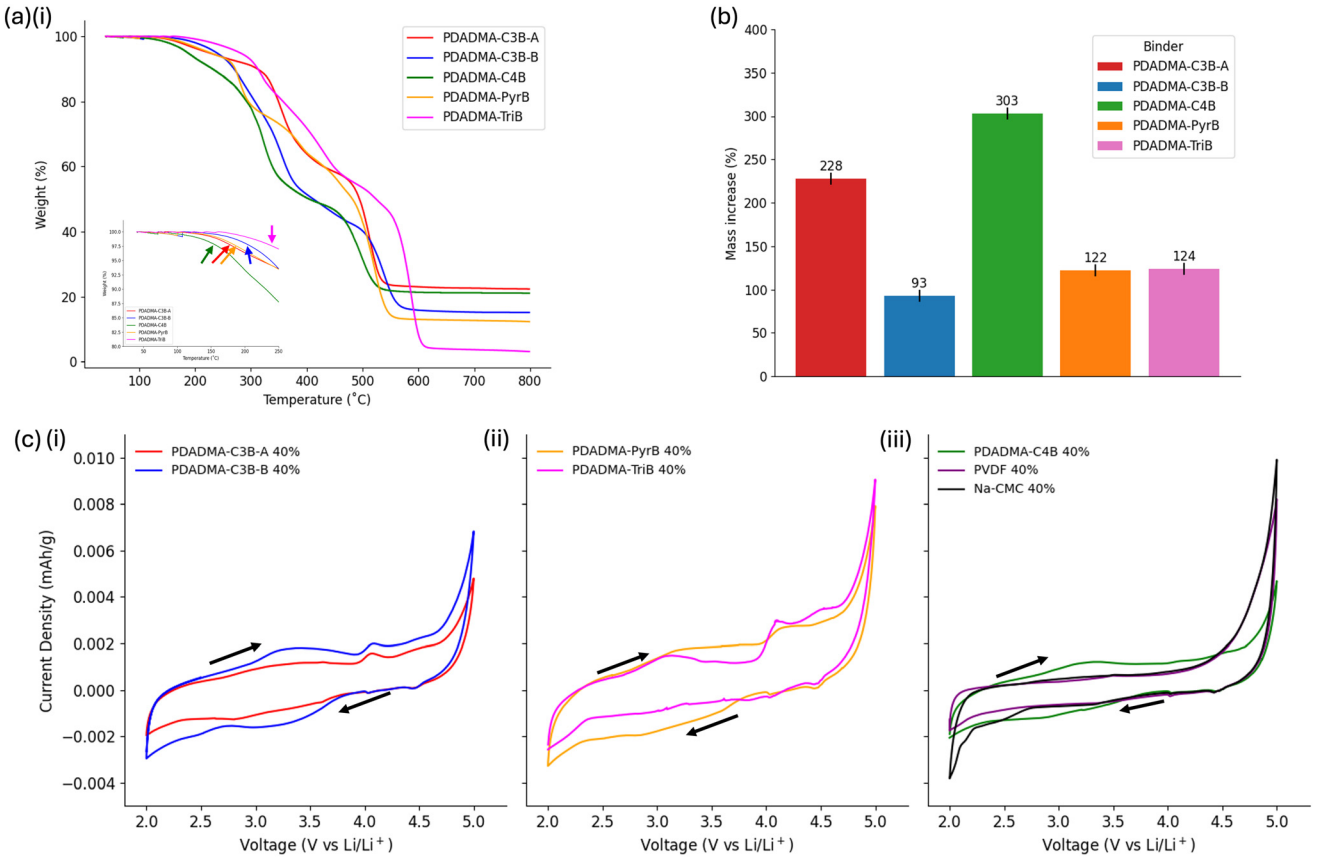

Fig. 3 (a) (i) TGA profiles of the PDADMA–borates from 25 to 800 °C heating at 10 °C min^{-1}, with an inset figure (25 to 250 °C) showing the onset of 2% mass loss for each binder, (b) mass uptake of electrolyte solution, 1 M $LiPF_6$ in EC : DEC (1 : 1), by the polymer binders after five days of immersion at room temperature, and (c) (i–iii) cyclic voltammetry (CV) profiles of the coin cells incorporating 40 wt% PDADMA–borates 60 wt% conductive carbon and lithium metal electrodes and 1 M Li[PF_6] in EC : DEC (1 : 1) electrolyte, sweeping at 0.1 mV s^{-1} between 2–5 V *vs.* Li/Li^+ (arrowheads indicate scan direction).

7%, respectively.[15] It is important to note electrolyte uptake was quantified only for 1 M $LiPF_6$ in EC : DEC; uptake in 1 M LiTFSI in DOL : DME and in 1 M LiTFSI [C_4mpyr][TFSI] (1 : 4) remains for future investigation.

While PDADMA–C4B exhibited the highest electrolyte uptake (303%), it is important to note that increased uptake does not inherently lead to better electrochemical performance. In conventional electrodes, ionic conductivity is largely determined by the engineered porosity of the electrode (typically up to 30 vol%), which facilitates ion pathways. This contrasts with solid-state systems, where the binder plays a dual role as the electrolyte medium and ion pathway.

Electrochemical stability

Before PDADMA–borate binders can be used in lithium battery applications, it is essential to evaluate their electrochemical stability within the relevant potential range. This stability was assessed using cyclic voltammetry (CV) in coin cells that did not contain the active material (NMC622). The working electrode was composed of 40 wt% PDADMA–borate and 60 wt% conductive carbon (C45), while lithium metal was used as both the counter and reference electrode. Cyclic voltammograms of PDADMA–borate binders display only minor anodic and cathodic currents at 3.0, 4.0 and 4.3 V *vs.* Li/Li^+ (Fig. 3(c) (i–iii)). Crucially, identical peaks appear in PVDF and Na-CMC control electrodes, indicating that these currents arise from redox processes of the C45 conductive carbon additive rather than binder decomposition. Nevertheless, the persistence of small currents near 4 V suggests partial oxidative processes at high potential, underscoring that while PDADMA–borates are broadly stable, they are not entirely electrochemically inert under these conditions. Similar behaviour has been reported for PDADMA-based PILs cycling up to 4 V, where minor carbon-related currents—but no binder degradation—were observed.[25,26]

Interestingly, the presence of N–H groups in PDADMA–C4B and PDADMA–C3B-A does not compromise electrochemical stability, as evidenced by the absence of significant reduction peaks in their cyclic voltammetry (CV) profiles (Fig. 3(c) (i) and (iii)). Furthermore, PDADMA–C3B-B, which lacks N–H functionalities, demonstrates competitive performance. This behaviour may be attributed to the inherent stability of its 5-membered ring structure, which

could provide greater rigidity compared to 6-membered alternatives.

For a direct comparison, the CV of 40 wt% PVDF and Na-CMC is also shown in Fig. 3(c) (iii). Both commercial binders show negligible anodic or cathodic currents across the 2–5 V window, confirming that the slight redox activity observed in the PDADMA–TriB and PDADMA–PyrB systems arises from binder oxidation rather than the carbon additive.

To further investigate stability at lower binder concentrations, the amount of PDADMA–borate in the working electrode was reduced to 20 wt% and 5 wt%, with C45 adjusted to 80 wt% and 95 wt%, respectively. This adjustment was made to simulate typical battery applications conditions, where the binder content generally ranges from 2–5 wt%.[27] CVs for the PDADMA–borate binders in these lower weight ratios are shown in the SI (Fig. S31 and S32). The CV profiles in these figures closely resemble those in Fig. 3(c) (i–iii), with the only notable difference being an increase in current density. This suggests that the binders remain stable and are suitable for electrode processing at low weight ratios. The observed increase in current density with higher carbon content can be attributed to the larger electrode surface area, which facilitates electrochemical reactions. Although C45 may exhibit catalytic properties, the primary effect is likely due to increased surface availability.

To further evaluate the electrochemical stability, two additional electrolytes (1 M Li[TFSI] in DOL : DME (1 : 1) and [C_4mpyr][TFSI] (1 : 4)) were tested, with corresponding CV results available in the SI (Fig. S33 and S34). Across all electrolyte systems investigated, the PDADMA–borate binders demonstrated consistent electrochemical stability, showing no significant redox reactions in the 2–5 V *vs.* Li/Li^+ range.

Adhesion properties

Adhesion characteristics of the PILS were examed using a peeling test for electrodes with a working composition of 90 wt% NMC622, 5 wt% C45, and 5 wt% PDADMA–borate binder. Electrode slurries were prepared in water, cast onto a carbon-coated aluminium current collector and allowed to dry. Once dried, peeling tests were performed to determine the effectiveness of the PIL binders on adhesion between the active layer (NMC622, C45 and PDADMA–borate) and the current collector. The peeling test (Fig. S35 in the SI) revealed the following order; PDADMA–C4B (2.4 N) > PDADMA–C3B-A (1.9 N) > PDADMA–C3B-B (1.4 N) > PDADMA–TriB (0.7 N) > PDADMA–PyrB (0.2 N). PDADMA–C4B and PDADMA–C3B-A gave higher adhesion strength than that found in comparative tests with PVDF (1.8 N). However, all of the PDADMA–borate binders showed weaker adhesion strength than that obtained using Na-CMC (4 N).

Electrochemical measurements

Electrochemical measurements, including IV and galvanostatic cycling, were performed using the same coin cell configuration to evaluate the NMC622 cathodes with the different binders. The internal resistance was determined before cycling by plotting the voltage against the current, with the gradient of the resulting line representing the internal resistance.

Internal resistance was measured following the experimental protocol outlined by Vauthier *et al.*,[13] using a two-probe configuration. This method captures both ionic and electronic resistance contributions based on the slope of voltage–current plots. The test consists of five main steps: (1) activation, where the cell is charged galvanostatically at C/3 from open circuit voltage (SOC = 0%) to 4.3 V, followed by a discharge–charge cycle; (2) capacity check, in which the actual cell capacity is determined through a discharge–charge cycle at C/3; (3) SOC adjustment to 56%, chosen for its stable voltage region to minimise measurement errors; (4) IV measurement, where a series of current pulses (0.3C, 1C, 3C, and 5C) are applied for 10 seconds, and the voltage drop for each pulse is recorded; and (5) final discharge to SOC = 0%. An example voltage–time profile obtained during the internal resistance measurement is presented in Fig. S36. The internal resistance is calculated from the slope of the voltage drop *versus* current curve (Fig. S37 and S38), providing insight into the total resistance of the cell, including binder-related effects. The trend in internal resistance with the PIL binders is as follows: PDADMA–C4B (0.8 Ω mg_{NMC}^{-1}, 13.8 Ω cm^2) < PVDF (0.9 Ω mg_{NMC}^{-1}, 15.5 Ω cm^2) < Na-CMC (1.2 Ω mg_{NMC}^{-1}, 20.6 Ω cm^2) < PDADMA–C3B-B (2.9 Ω mg_{NMC}^{-1}, 49.9 Ω cm^2) < PDADMA–PyrB (3.8 Ω mg_{NMC}^{-1}, 65.4 Ω cm^2) < PDADMA–C3B-A (8.2 Ω mg_{NMC}^{-1}, 141.0 Ω cm^2) < PDADMA–TriB (29.5 Ω mg_{NMC}^{-1}, 507.4 Ω cm^2) and is shown in the SI (Fig. S39).

High internal resistance significantly impedes lithium transport, limiting the battery's ability to deliver high currents. This occurs because of increased polarisation resistance during cycling, which causes the electrode potential to deviate from equilibrium, ultimately decreasing overall battery performance. Among the binders tested, PDADMA–C4B exhibited the lowest resistance, indicating the potential for superior cycling performance. In contrast, PDADMA–TriB demonstrated the highest resistance, suggesting reduced cycling efficiency.

A correlation between resistance and electrolyte uptake can be observed (Fig. 3(b)). PDADMA–C4B demonstrated the highest electrolyte uptake (303%), which reduced the ionic resistance by providing a continuous pathway for ion transport, resulting in the lowest internal resistance. Although PDADMA–TriB showed a more moderate electrolyte uptake (124%), it exhibited the highest resistance, indicating other limiting factors may be at play. Interestingly, the binder with the lowest electrolyte uptake, PDADMA–C3B-B (93%), showed an internal resistance of 2.9 Ω mg_{NMC}^{-1}, which was only slightly higher than that of Na-CMC (1.2 Ω mg_{NMC}^{-1}). This suggests that while electrolyte uptake is a key factor in determining internal resistance, other properties of the binder, such as its ionic conductivity or interfacial compatibility, may also influence performance.

A molecular insight into these five binders show that the two O/N-chelated borates (C4B, C3B-A) have high electrolyte uptake (303% and 228% uptake, Fig. 3(b)) as well as broad electrochemical stability (no redox peaks to 5 V, Fig. 3(c) (i–iii)). Whereas the fully azolyl anions (PyrB, TriB) show only moderate swelling (122–124%) and emerging oxidation currents above 4.5 V. This could be due to the stronger coordination environment in the alkanolamine-derived borates, which both solvate Li^+ effectively and resist oxidative decomposition.

The presence of polar N–H groups in C4B and C3B-A enhances electrolyte uptake *via* hydrogen-bonding to EC/DEC, yielding continuous ion-transport pathways and thus lower internal resistance (0.8 Ω mg_{NMC}^{-1} for C4B *vs.* 0.9 Ω mg_{NMC}^{-1} for PVDF; Fig. S39). By contrast, the N-heterocycle-only binders lack these H-bond donors and display higher resistances (3.8–29.5 Ω mg_{NMC}^{-1}).

Although the five-membered chelate in C3B-B gives greater backbone rigidity relative to C3B-A, its lower electrolyte uptake (93% *vs.* 228% for C3B-A) limits the formation of continuous ion-conducting domains. As a result, despite moderate peel strength, C3B-B exhibits only intermediate internal resistance (2.9 Ω mg_{NMC}^{-1}). This highlights that optimal performance requires a balance between polymer rigidity (for film integrity), sufficient swelling (for ion transport) and strong interfacial adhesion.

These molecular-level insights suggest that an ideal binder will combine a robust O/N-chelation motif—so that the borate anion remains coordinated and resists oxidation—with polar N–H functionalities that promote hydrogen bonding to EC/DEC and thereby maximise electrolyte uptake and minimise ionic resistance. At the same time, the rigidity of the chelate ring must be carefully tuned—too flexible a six-membered system swells excessively and raises resistance, whereas a smaller five-membered ring limits swelling but still preserves a continuous ion-transport network. By weaving together strong chelation, H-bonding sites and controlled backbone rigidity, it is possible to achieve a binder that simultaneously delivers outstanding rate capability and cycle stability.

Galvanostatic cycling

Galvanostatic cycling of the NMC622 cathodes prepared with the different PDADMA–borate binders and lithium anodes

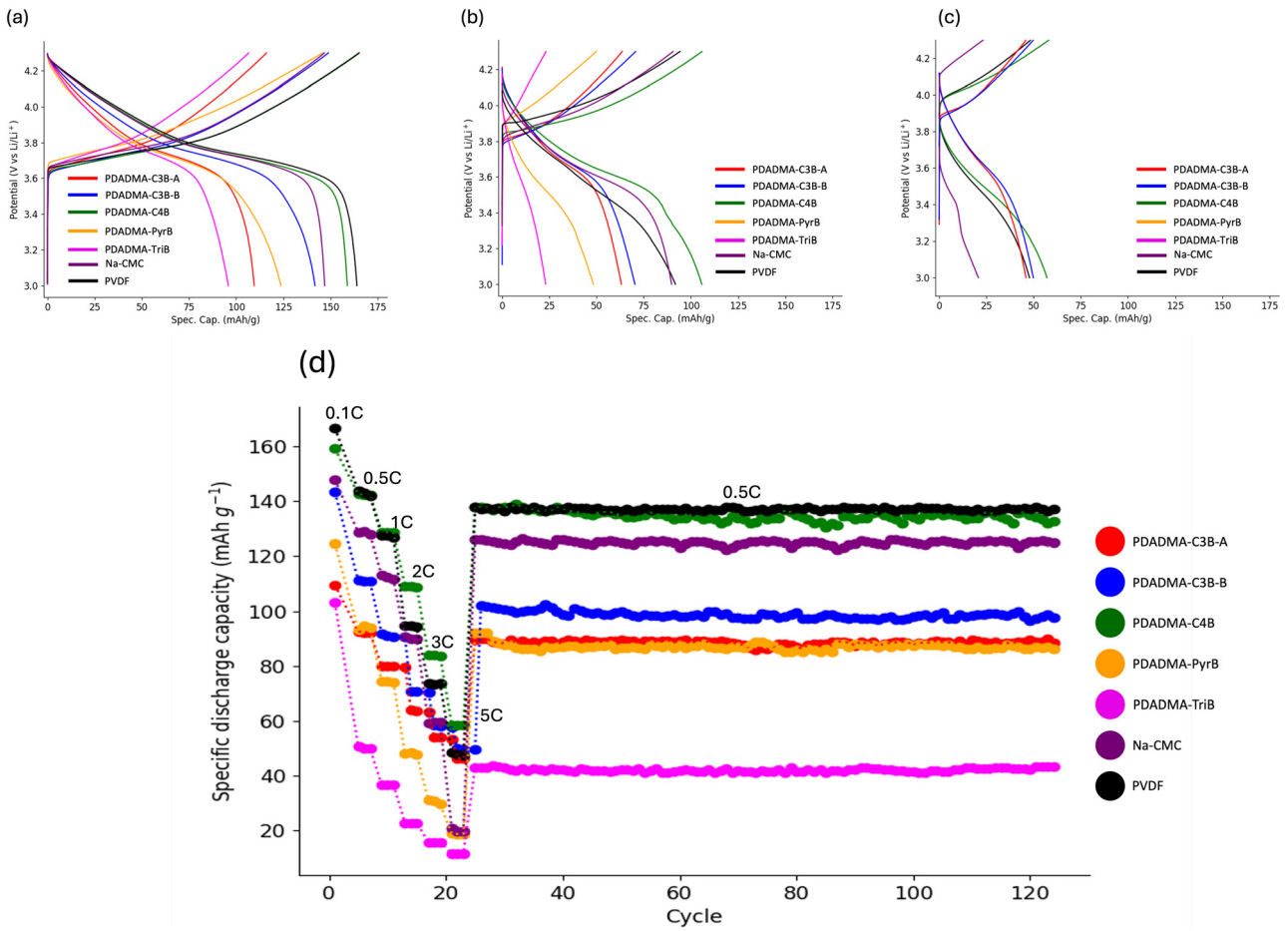

Fig. 4 (a) Cycling performance of NMC622 cathode and lithium anode using different binders at 0.1C (fourth cycle). (b) Cycling performance of NMC622 cathode and lithium anode using different binders at 2C (fourth cycle). (c) Cycling performance of NMC622 cathode and lithium anode using different binders at 5C (fourth cycle). (d) Cycling performance for 100 cycles at 0.5C using different binders.

was performed at C-rates of 0.1C, 0.5C, 1C, 2C, 3C, and 5C with five cycles at each C-rate. Fig. 4(a)–(c) show the voltage profiles from the fourth cycle at 0.1C, 2C, and 5C respectively with each binder and can be compared to the practically achievable capacity of NMC622 (175 mAh g^{-1}).[28] At a low C rate of 0.1C, cathodes containing benchmark PVDF and PDADMA–C4B as binders both show capacities close to the theoretical specific capacity of NMC622 (175 mAh g^{-1}), with the PVDF-containing cathode having the highest performance (164 mAh g^{-1}) closely followed by PDADMA–C4B (159 mAh g^{-1}). In contrast, PDADMA–C3B-A, PDADMA–PyrB, and PDADMA–TriB all resulted in lower cycling performances of 109 mAh g^{-1}, 124 mAh g^{-1}, and 96 mAh g^{-1} respectively. This low cycling performance could be due to poor dispersion of the binder material, which generates an inefficient conductive network within the electrode. This would impact the kinetics of electron transport, which can reduce the electrode's rate capability. In some cases, it can potentially cause cracks to form in the electrode, this can lead to a loss of contact between particles which can significantly decrease the capacity of the cell.

At 0.5C, the discharge capacities of the cells with PDADMA–C4B and PVDF binders were very similar at 142.6 mAh g^{-1} and 143.2 mAh g^{-1} respectively and when the C-rate was increased further to 1C, PDADMA–C4B starts to slightly outperform PVDF showing capacities of 128.7 ± 0.3 mAh g^{-1} and 127.5 ± 0.4 mAh g^{-1} respectively. At higher C-rates of 2C, 3C, and 5C, the PDADMA–C4B binder outperforms PVDF and the cell with a cathode containing PDADMA–C4B shows higher discharge capacities of 108.9 mAh g^{-1}, 84.0 mAh g^{-1}, and 58.3 mAh g^{-1} compared to PVDF where the corresponding discharge capacities were 94.8 mAh g^{-1}, 73.7 mAh g^{-1}, and 47.7 mAh g^{-1}.

The results at higher C-rates (2C and 5C) highlight the performance advantages of the PDADMA-based binders over the conventional PVDF binder under demanding conditions. At 2C (Fig. 4(b)), all binders show a decline in discharge capacity, but PDADMA–C4B stands out with a capacity of 107 mAh g^{-1}, surpassing PVDF, which only achieves 92 mAh g^{-1}. This suggests that PDADMA–C4B maintains better structural integrity or lithium-ion accessibility during faster charging/discharging cycles, allowing it to sustain higher capacities.

At the more rigorous 5C rate (Fig. 4(c)), where high power demand typically exacerbates capacity loss, both PDADMA–C4B and PDADMA–C3B-B continue to outperform PVDF. PDADMA–C4B achieves the highest discharge capacity at 57 mAh g^{-1}, followed by PDADMA–C3B-B at 50 mAh g^{-1}, while PVDF trails at 47 mAh g^{-1}. These results suggest that the PDADMA-based binders provide superior electrochemical stability and efficiency at high C-rates, making them more suitable for applications requiring rapid energy discharge and recharge. Notably, the PDADMA–C4B cells exhibit small cycle-to-cycle capacity fluctuations (<3%) at 5C. These minor ionic-transport variations could be due to the polymer network under extreme rates. Importantly, these fluctuations do not compromise the overall high-rate performance of PDADMA–C4B.

The current density was then returned to 0.5C, and long-term cycling (100 cycles) was performed to determine whether the binders could achieve stable cycling performance at 0.5C. Fig. 4(d) shows that all the binders gave stable cycling performance for 100 cycles with no reduction in the discharge capacity from the first to the 100th cycle. At 0.5C, the order of the best-performing binder to the least is PVDF ≈ PDADMA–C4B > Na-CMC > PDADMA–C3B-B > PDADMA–C3B-A ≈ PDADMA–PyrB > PDADMA–TriB. This ordering is consistent with the results from IV measurement described above, with the least resistant binder (PDADMA–C4B) showing the best performance while the most resistant binder (PDADMA–TriB) having the poorest performance. The only slight deviation from this order is with PDADMA–PyrB that is less resistant than PDADMA–C3B-A but PDADMA–C3B-A showed better cycling performance than PDADMA–PyrB. A number of experimental factors, including temperature, electrode distance, state of charge *etc.* may contribute to these variations.[29]

The capacity retention achieved for each binder is summarised in Table 1. PDADMA–C4B showed better capacity retention and improved cycling performance when compared to Na-CMC. The other PDADMA–borate binders examined display either capacity retentions similar to or lower than that with Na-CMC. Many factors can affect a cell's discharge capacities and retention capacity such as cell type, loading, porosity, electrolyte, cycling procedure, cell history, rest period temperature, *etc.*[30]

The best performing PDADMA–borate binder (PDADMA–C4B) was tested with another common lithium cathode material LFP ($LiFePO_4$). The LFP electrode was prepared in the same manner as described for the NMC electrodes and lithium metal was used as anodes. The C-rates at which the LFP cell was cycled were; 0.1C, 0.5C, 1C, 2C, 3C, and 5C, after which 100 cycles were performed at 1C. The performance of the PDADMA–C4B binder was compared to Na-CMC and PVDF, which can be found in the SI (Fig. S40). PDADMA–C4B not only outperformed Na-CMC but also outperformed PVDF at all C-rates. When cycled at 1C for 100 cycles PDADMA–C4B showed a discharge capacity of 147.0 mAh g^{-1}, while PVDF and Na-CMC showed discharge capacities of 130.0 mAh g^{-1} and 83.0 mAh g^{-1} respectively.

Table 1 The capacity retention (%) of the NMC622 cathode using different binders at 0.5C after 100 cycles

Binder	Capacity retention (%)
PDADMA–C3B-A	71.1
PDADMA–C3B-B	80.0
PDADMA–C4B	89.5
PDADMA–PyrB	70.1
PDADMA–TriB	65.9
PVDF	96.5
Na-CMC	81.0

Interestingly, PDADMA–C4B not only matches PVDF in LFP but actually exceeds it at all C-rates, suggesting good chemical compatibility with the phosphate framework. By contrast, oxide cathodes such as NMC622 cycle at higher potentials (up to 4.3–4.5 V) and involve more redox-active transition metals, which place greater demands on binder–electrode interphases. The slightly lower initial capacity and more pronounced rate-dependent losses we observe in NMC622 can be due to subtle differences in interfacial stability and ionic transport: in oxides, the binder must both resist oxidative attack and maintain continuous Li^+ pathways through a more reactive surface, whereas in LFP cathodes the surface chemistry is inherently less aggressive. These mechanistic distinctions could help explain why PDADMA–C4B delivers such outstanding performance in phosphate systems and yet still achieves competitive results in NMC622, highlighting its versatility across diverse cathode materials.

Surface characterisation of cathodes

Many factors can affect a cell's discharge capacities and retention capacity.[29,30] A possible way to understand why these binders perform so differently electrochemically when used with the NMC622 cathode is to perform surface characterisation such as scanning electron microscope (SEM) with elemental mapping by energy dispersive X-ray spectroscopy (EDX) on the cathodes before and after cycling.

Scanning electron microscope (SEM) measurements were performed on the surface of the electrodes before and after cycling to determine whether there were any physical changes to the electrodes before cycling and attempt to explain the different electrochemical behaviours. The low magnification images (Fig. S41 in the SI) of the pristine PDADMA–C4B, PDADMA–C3B-B and PVDF electrodes show an evenly distributed morphology on the surface. In contrast, the other electrodes, with Na-CMC, PDADMA–C3B-A, PDADMA–PyrB, and PDADAM–TriB binders, show an uneven morphology resulting in voids on the surface, the voids could be an explanation for the poor electrochemical performance.

On increased magnification (Fig. S42 in the SI) the voids can be observed to be more prominent, particularly for PDADMA–PyrB, PDADMA–TriB, and Na-CMC, while the remaining show an even distribution of the material. Additionally, PVDF and all of the PDADMA–borate binders depict spherical-like active material particles, whereas Na-CMC show unique active material morphologies with particles that are cracked, contain splits, or are flattened and compressed.

Comparing the SEM images of the pristine electrodes (Fig. S41) with those of the aged electrodes (Fig. 5), PVDF, PDADMA–C4B, and PDADMA–PyrB all show no significant changes in the morphology of the particles. In contrast, PDADMA–TriB and PDADMA–C3B-A showed what seems to be small formations of voids. These voids are unlikely to be due to splitting or cracking of the NMC622 within the composite electrode due to their scale and could be due to decomposition of salts or the electrolyte. The main difference in the SEM images is seen when the Na-CMC and PDADMA–borates systems are compared, with the PDADMA–borates showing no significant changes in appearance between pristine and aged electrodes whereas with Na-CMC as binder, extensive cracking or splitting of the NMC622 particles after cycling is observed leading to significantly great damage to the electrode surface.

Energy dispersive X-ray (EDX) measurements on the electrodes (Fig. S43 in the SI) showed the presence of the elements for the appropriate binders. Unfortunately, boron was too light to detect and so it was not analysable. However, the elements oxygen, nitrogen, and carbon (carbon highlighted in the EDX measurements shown in Fig. S43 in the SI) present in the ligands around the boron centre were

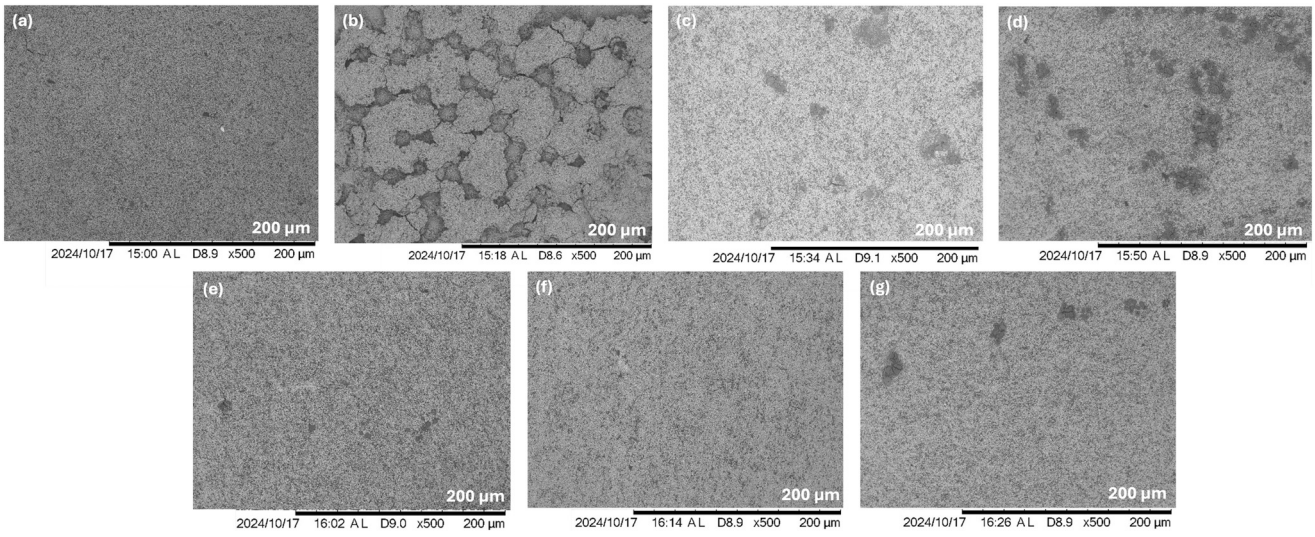

Fig. 5 Surface SEM images of the aged NMC622 electrodes (a) PVDF, (b) Na-CMC, (c) PDADMA–C3B-A, (d) PDADMA–C3B-B, (e) PDADMA–C4B, (f) PDADMA–PyrB, (g) PDADMA–TriB.

detected, suggesting that the materials are well distributed and there are no clusters of conductive carbon.

To further characterise the surface composition of the electrodes, XPS was performed on aged NMC622 cathodes using only the best-performing binder (PDADMA–C4B) and commercially-available PVDF. Neither spectrum exhibited detectable signals from Ni, Mn, or Co, suggesting a thick layer (>10 nm) was deposited over the cathode during cycling.

Both electrodes showed broadly similar surface chemistries, with the most pronounced difference appearing in the F1s region (Fig. 6). For the PVDF-based electrode (Fig. 6(a)), two deconvoluted components appear at 684.9 eV—assigned to LiF formed during cycling—and at 686.5 eV—assigned to the C–F bonds of the PVDF binder. In contrast, the PDADMA–C4B electrode (Fig. 6(b)) also shows a LiF component at 684.8 eV, but its intensity is substantially lower, and a second component at 686.7 eV, which we attribute to $Li_xPO_yF_z$ species in the SEI formed from $LiPF_6$ decomposition (*e.g.* $LiPO_2F_2$, $LiPF_2O_2$).[31] The peak intensity of LiF in Fig. 6(b) is significantly less than that in Fig. 6(a), which suggests a reduced formation of LiF. This correlates with the superior high C-rate performance, as excessive formation of LiF is known to impede Li^+ ion transport, increasing interfacial resistance and reducing capacity at high C-rates.[32]

The B1s/Cl2p XPS of the PDADMA–C4B based cathode is shown in Fig. 6(c). A peak at 191.4 eV is likely due to the formation of inorganic borate/borophosphate (*e.g.* Li_3BO_3 or $Li_xB_nO_mF_y$) which may have formed *via* the reaction of the C4B anion with $[PF_6]^-$ decomposition products.[33,34] A second, less intense peak is seen at 194.2 eV, which also corresponds to a boron species, but a fluorinated species (*e.g.* BF_xO_y).[35] The final two small peaks seen are at 198.3 eV and 200.1 eV, both of which arise from residual PDADMA–Cl, indicating incomplete anion exchange during synthesis.[36] Nonetheless, the predominance of the 191.4 eV component suggests that there is a strong presence of boron based inorganic species on the surface, while the minor fluoroborate and chloride signals reflect electrolyte decomposition and trace synthesis impurity, respectively.

Conclusion

In conclusion, we present the successful synthesis and characterisation of five water-soluble and fluorine-free PDADMA–borate poly(ionic liquids). Thermal analysis reveals promising stability, with decomposition temperatures exceeding 150 °C. Electrolyte uptake studies indicate that these binders possess significant swelling capabilities, especially PDADMA–C4B and PDADMA–C3B-A that

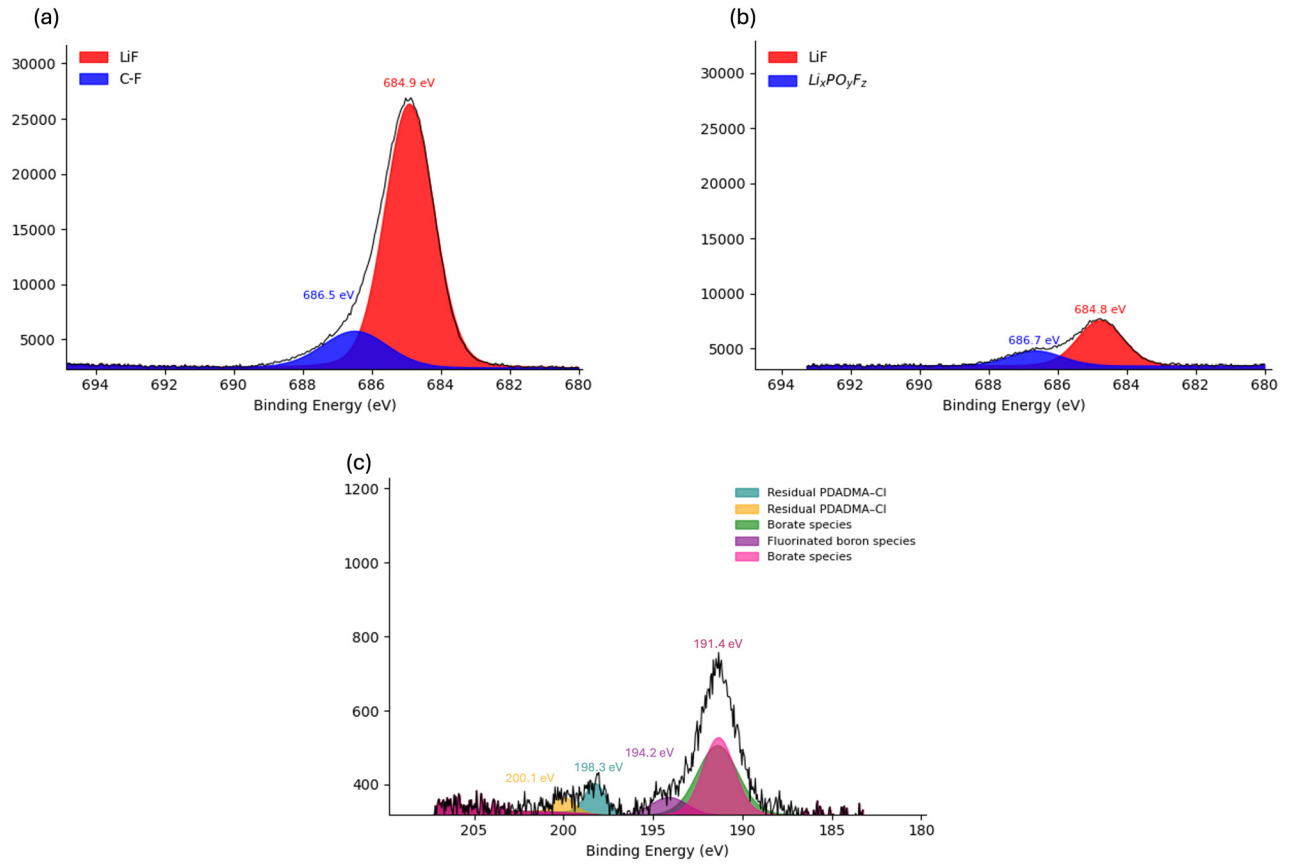

Fig. 6 XPS spectra of the aged NMC622 cathodes in the F1s region (a) PVDF, (b) PDADMA–C4B, and (c) XPS spectra in the B1s/Cl2p region for PDADMA–C4B electrode.

incorporate O/N-chelated orthoborate anions derived from alkanolamines. Swelling and uptake of electrolyte solutions enhances ion transport pathways. The electrochemical stability, as assessed through cyclic voltammetry, showed no significant redox activity in the desired voltage range, in three separate electrolyte systems indicating compatibility with lithium cycling.

The different PDADMA borates were used as binders for the aqueous processing of lithium ion battery electrodes. When incorporated into NMC622 cathodes, PDADMA–C4B displayed excellent cycling performance and capacity retention, that rivals and even outperforms conventional binders such as PVDF and Na-CMC. PDADMA–C4B, demonstrated enhanced electrochemical properties across various C-rates and outperformed PVDF when incorporated into LFP cathodes, indicating its potential for broader applications in different lithium cathode materials. The morphological analysis *via* SEM suggested that the structural integrity of the electrodes was maintained over repeated cycling. Furthermore, based on the XPS results, we hypothesise that the borate counter-anions in PDADMA binders may promote the formation of inorganic-rich interphase films on electrode surfaces, enhancing battery stability and performance.

Looking forward, several directions for future work are evident. Evaluating PDADMA–C4B in full-cell configurations, such as NMC622|graphite pouch cells, would enable more practical benchmarking under commercial-like conditions. Tensile testing of dry and swollen films to quantify mechanical robustness under electrolyte uptake. A comprehensive matrix screening of PIL formulations (as a function of anion) and electrolyte compositions, including different metal-salt cations/anions and solvent systems, is planned to identify optimal combinations for enhanced uptake, conductivity, and stability. These materials will then be associated with further cell testing. Additionally, extending this work to higher-voltage cathodes such as NMC811, particularly under elevated cut-off voltages (*e.g.*, 4.5 V), would further test the electrochemical robustness of the borate-based binders. Finally, given the water-processable nature and ionic conductivity of these binders, their application in sodium-ion battery systems—such as NVPF|HC—represents a promising area for future investigation.

Overall, these results suggest that PDADMA–borate binders, particularly PDADMA–C4B not only provide an environmentally friendly alternative to traditional fluorinated binders but are promising candidates for use as binders in LIBs, demonstrating both superior electrochemical performance and stability, which could lead to advancements in battery technology.

Experimental section

Materials

Boric acid, sodium borohydride, 3-amino-1-propanol, 2-amino-2-methyl-1-propanol, 2-(methylamino)ethanol, 1,2,4-triazole, poly(diallyldimethylammonium chloride) (PDADMA–Cl, 400 000–500 000 molecular weight, 20 wt% in water), poly(vinylidene fluoride) (PVDF), and sodium carboxymethyl cellulose (Na-CMC) were used as received from Sigma-Aldrich. Pyrazole was used as received from Doug Discovery (Fluorochem).

Conductive carbon (C45) was purchased from Imerys, and ($LiNi_{0.6}Mn_{0.2}Co_{0.2}O_2$) (NMC622) was purchased from Targray, which was composed of polycrystalline particles with diameters of 10–12 μm. The battery-grade foil was purchased from Cambridge Energy Solutions. All three were used as received.

Characterisation

^1H, ^{13}C, and ^{11}B NMR spectra were recorded in D_2O at ambient temperature on a Bruker Avance III 400 MHz spectrometer. IR spectra were recorded on a Bruker Alpha II FT-IR spectrometer under ambient conditions. Thermal properties were determined using a TA Instruments TGA Q500 thermogravimetric analyser under a nitrogen atmosphere at a rate of 10 °C min^{-1} from 25 °C to 800 °C.

The uptake of electrolyte by the polymer binders was investigated by immersing the binder in the electrolyte solution (1 M $Li[PF_6]$ in EC : DEC (1 : 1)) for five days within an Ar glovebox to avoid ambient moisture. Electrolyte uptake was quantified only for 1 M $LiPF_6$ in EC : DEC; uptake in 1 M LiTFSI in DOL : DME and in LiTFSI [C_4mpyr][TFSI] (1 : 4) remains for future investigation. After five days' immersion, excess electrolyte was gently removed by patting the films with lint-free tissue before immediate weighing. The weight increase was monitored and calculated using eqn (1).

$$\text{mass increase (\%)} = \frac{m_1 - m_0}{m_0} \times 100 \quad (1)$$

where m_0 is the mass before immersion and m_1 is the mass after immersion.

The coin cells were constructed in an argon glovebox. Each coin cell was prepared using a 10 mm diameter NMC622 cathode punched from battery-grade foil, with the composition of the cathode being 90 wt% NMC622, 5 wt% C45, and 5 wt% binder. The total areal loading is 19.10 mg cm^{-2} (17.2 mg cm^{-2} active NMC622). As the electrodes had the same loading, a theoretical porosity of 53% ± 2 was obtained for the electrodes. The small variations in the porosity are due to the change in binder density, as no calendaring of electrodes was performed. The lithium metal anode was prepared by punching a 12 mm diameter disk from a lithium foil. A 16 mm glass fiber type (Whatman GF/A) separator and 200 μl of electrolyte were used.

Electrochemical characterisation

Cyclic voltammetry (CV) on the polymers was conducted using a VMP-3 potentiostat (Biologic Science Instruments) in the range of 2.0–5.0 V (*vs.* Li/Li^+) at 0.1 mV s^{-1}. A volume of

200 μl of 1 M $LiPF_6$ in a 1 : 1 mixture of ethylene carbonate (EC) and diethyl carbonate (DEC) was used as the electrolyte.

Electrochemical measurement

Cathodes were prepared by making a slurry, casting and then drying the electrodes. As it is known the most commonly used binder is PVDF which is not only fluorinated but also requires the toxic organic solvent *N*-methyl-2-pyrrolidone (NMP) during the slurry mixing. When replacing the PVDF binder with the PDADMA–borates reported here, not only are they fluorine-free, but are also water-soluble. This allows for safer and cheaper preparation of the electrodes and also allows for a lower drying temperature compared to when NMP was used. The slurries were prepared by first dissolving the binder (20 mg) in 0.2 ml of solvent (water for PDADMA–borates and NMP for PVDF). Once dissolved C45 (20 mg) and NMC622 ($LiNi_{0.6}Mn_{0.2}Co_{0.2}O_2$) (360 mg) was added to the solution, and the mixture was thoroughly mixed using a centrifugal mixer (3000 rpm, 2 minutes). The thick slurry was then cast using a doctor blade technique with a thickness of 180 μm onto a carbon-coated aluminium current collector. The electrodes were then dried overnight at 60 °C. After drying, 10 mm diameter discs were punched from the NMC622 cathode, and the cathodes were further dried in a vacuum oven overnight at 60 °C, before being transferred into a glovebox. This meant the total areal loading is 19.1 mg cm^{-2} of which 17.2 mg cm^{-2} corresponds to active material (NMC622, 90 wt%). The minimal amount of water and extensive drying and storage under an inert atmosphere helped avoid Li-leaching and NMC degradation.

It is important to note that the densities of the binders differ, so a fixed 5 wt% binder corresponds to approximately 5 ± 0.5 vol% in each electrode. This minor variation in binder volume fraction is unlikely to affect the comparative performance trends reported. The cycling performance was compared against cathodes prepared using the well-known water-soluble binder, Na-CMC, and with PVDF, both at the same composition as electrodes incorporating the PDADMA–borates.

Galvanostatic charging and discharging cycles were conducted on the NMC622|lithium coin cells, using a Neware battery cycler, in a voltage range of 3–4.3 V (*vs.* Li/Li^+). In all cases 200 μl of 1 M $Li[PF_6]$ in EC : DEC (1 : 1) electrolyte was used. After two hours of rest at open-circuit potential, the electrochemical response was tested at different C-rates: 0.1C, 0.5C, 1C, 2C, 3C, 5C and long-term cycling over 100 cycles at 0.5C. Scanning electron microscope (SEM) images of the cathodes before and after cycling were recorded. After galvanostatic cycling, the coin cells were disassembled inside a glovebox, and the cathodes were washed with dimethyl carbonate (DMC) to remove any remaining salts on the surface. The SEM images were recorded using a Hitachi TM3030 series tabletop microscope at an accelerating voltage of 2 kV and an energy dispersive X-ray spectrometer (EDX) attached to the microscope.

X-ray photoelectron spectroscopy (XPS) measurements were performed on a Versaprobe III AD Physical Electronics (ULVAC) system with monochromatic radiation source Al Kα (1486.7 eV). An initial analysis was carried out to determine the elements present (wide scan: step energy 0.2 eV, pass energy 224 eV) then a detailed analysis of the detected elements was performed (detail scan: step energy 0.05 eV, pass energy 27 eV, time per step 20 ms) with an electron output angle of 45°. The spectrometer was previously calibrated with Ag (Ag 3d5/2, 368.26 eV). The spectra were adjusted using CasaXPS 2.3.26 software, which models contributions after a background subtraction (Shirley).

Preparation of acid (H^+) borates

$H[B(C_4H_9NO)_2]$. Boric acid (5.4 g, 80.95 mmol) and 2-amino-2-methylpropan-1-ol (16 ml, 161.73 mmol) were combined in toluene (100 ml). The mixture was then heated at 125 °C for 8 hours, collecting evolved water in a Dean–Stark condenser. The remaining toluene was then removed *via* rotary evaporation, then dried overnight under high vacuum at 80 °C, to give a white waxy solid with a yield of 9.69 g, 80.9%. This method was repeated for the remaining acid O/N-chelated borates. ^1H (400 MHz, D_2O) δ 3.25 (4H, s, O–C$\mathbf{H}_2$–), 0.98 (12H, s, C$\mathbf{H}_3$–C–); ^{13}C (100 MHz, D_2O) δ 69.94 (O–$\mathbf{C}H_2$), 51.18 (N–**C**–), 24.14 ($\mathbf{C}H_3$–C–); ^{11}B (128 MHz, D_2O) δ 4.48.

$H[B(C_3H_7NO)_2]$ (A). Boric acid (5.1 g, 80.89 mmol) and 3-aminopropan-1-ol (14 ml, 161.73 mmol) were used, this gave a cloudy waxy solid with a yield of 8.49 g, 83.6%. ^1H (400 MHz, D2O) δ 3.67 (4H, m, O–C$\mathbf{H}_2$–), 2.86 (4H, s, NH–C$\mathbf{H}_2$), 1.76 (4H, s, CH_2–C$\mathbf{H}_2$–CH_2); ^{13}C (100 MHz, D_2O) δ 59.33 (O–$\mathbf{C}H_2$), 37.40 (NH–$\mathbf{C}H_2$), 31.99 (CH_2–$\mathbf{C}H_2$–CH_2); ^{11}B (128 MHz, D_2O) δ 3.66.

$H[B(C_3H_7NO)_2]$ (B). Boric acid (5.0 g, 80.87 mmol) and 2-(methylamino)ethan-1-ol (13.5 ml, 161.73 mmol) were used, this gave a viscous liquid with a yield of 8.22 g, 80.9%. ^1H (400 MHz, D_2O) δ 3.74 (4H, s, O–$\mathbf{C}H_2$–), 2.90 (4H, s, N–$\mathbf{C}H_2$–), 2.52 (6H, s, N–C$\mathbf{H}_3$); ^{13}C (100 MHz, D_2O) δ 58.30 (O–$\mathbf{C}H_2$–), 51.15 (N–$\mathbf{C}H_2$–), 33.50 (N–$\mathbf{C}H_3$); 11B (128 MHz, D_2O) δ 3.90.

$H[B(pyrazole)_4]$. Sodium borohydride (3.00 g, 79.30 mmol) and pyrazole (27.00 g, 400 mmol) (1 : 5 ratio) were placed into a round bottom flask under nitrogen and heated to 125 °C. The evolution of hydrogen was monitored, and the reaction proceeded for 4 hours, after which the evolution of gas ceased. The reaction flask was cooled to room temperature, and acetone (100 ml) was added to extract the excess, unreacted pyrazole as well as any byproducts which are usually sodium borate salts that did not go to completion. This left the crude product which was filtered and dried overnight under a high vacuum at 80 °C, to give $Na[B(pyrazole)_4]$ as a white powder. This was then dissolved in 150 ml of distilled water and passed through a column containing a bed of the exchange resin Amberlite IR-120 collecting $H[B(pyrazole)_4]$. The water was removed and dried to give a white waxy solid. This method was repeated for

H[B(triazole)$_4$]. ^{1}H (400 MHz, D_2O) δ 7.66 (8H, s, –N–C**H**═, –N═C**H**–), 6.38 (4H, s, –CH═C**H**–); ^{13}C (100 MHz, D_2O) δ 137.48 (–N═**C**H–), 133.27 (–N–**C**H═), 101.89 (–CH═**C**H–); ^{11}B (128 MHz, D_2O) δ 3.56.

H[B(triazole)$_4$]. Sodium borohydride (3.00 g, 79.30 mmol) and 1,2,4-triazole (27.36 g, 400 mmol) were used after the solution was passed through a column and H[B(triazole)$_4$] was collected to give a cloudy waxy substance. ^{1}H (400 MHz, D_2O) δ 8.32 (8H, s, –N═C**H**–); ^{13}C (100 MHz, D_2O) δ 143.06 (–N–N═**C**H–), 125.02 (–N═**C**H–N–); ^{11}B (128 MHz, D_2O) δ 4.48.

Preparation of poly(diallyldimethylammonium borates) (PDADMA–B(N/O)$_2$)

PDADMA–[B(C$_4$H$_9$NO)$_2$]. 15 g of PDADMA–Cl were first diluted in 250 ml of distilled water and passed through a column containing a bed of the exchange resin Amberlite IRN78, collecting PDADMA–OH. In a separate flask, 4.14 g of H[B(C$_4$H$_9$NO)$_2$] was dissolved in 15 ml of water and added to 100 ml of the aqueous solution of PDADMA–OH. The mixture was allowed to stir for one hour at room temperature. Then, the water was removed by rotary evaporation and dried overnight under a vacuum at 60 °C obtaining PDADMA–[B(C$_4$H$_9$NO)$_2$] as a pale yellow solid. This was repeated for the remaining PDADMA borates. ^{1}H (400 MHz, D_2O) δ 3.83 (2H, s, C**H**$_2$–N$^+$), 3.45 (4H, s, O–C**H**$_2$), 3.24–3.14 (8H, m, –N–C**H**$_3$, C**H**$_2$–N$^+$), 2.70 (2H, s, –CH$_2$–C**H**–), 1.52–1.32 (4H, m, –C**H**$_2$–CH), 1.19 (12H, s, C**H**$_3$–C–); ^{13}C (100 MHz, D_2O) δ 70.28, 68.66, 53.95, 52.64, 26.51, 23.08; ^{11}B (128 MHz, D_2O) δ 5.72.

PDADMA–[B(C$_3$H$_7$NO)$_2$] (A). To 100 ml of an aqueous solution of PDADMA–OH, 3.52 g of H[B(C$_3$H$_7$NO)$_2$] (A) were used, PDADMA–[B(C$_3$H$_7$NO)$_2$] (A) was obtained as a pale orange solid. ^{1}H (400 MHz, D_2O) δ 3.84–3.78 (2H, s, C**H**$_2$–N$^+$, 4H, s, O–C**H**$_2$), 3.26–3.15 (8H, m, –N–C**H**$_3$, C**H**$_2$–N$^+$), 3.03 (4H, s, NH–C**H**$_2$), 2.71 (2H, s, –CH$_2$–C**H**–), 2.62 (4H, s, –C**H**$_2$–), 1.56–1.33 (4H, m, –C**H**$_2$–CH); ^{13}C (100 MHz, D_2O) δ 70.32, 57.53, 53.98, 50.87, 38.63, 33.11, 26.50; ^{11}B (128 MHz, D_2O) δ 5.76.

PDADMA–[B(C$_3$H$_7$NO)$_2$] (B). To 100 ml of an aqueous solution of PDADMA–OH and 3.52 g of H[B(C$_3$H$_7$NO)$_2$] (B) were used, PDADMA–[B(C$_3$H$_7$NO)$_2$] (B) was obtained as a yellow solid. ^{1}H (400 MHz, D_2O) δ 3.82 (2H, s, C**H**$_2$–N$^+$), 3.68 (4H, m, O–C**H**$_2$–), 3.26–3.15 (8H, m, –N–C**H**$_3$, C**H**$_2$–N$^+$), 2.87 (4H, s, N–C**H**$_2$–), 2.70 (2H, s, –CH$_2$–C**H**–), 1.77 (6H, s, N–C**H**$_3$), 1.53–1.32 (4H, m, –C**H**$_2$–CH); ^{13}C (100 MHz, D_2O) δ 70.29, 59.29, 53.96, 52.23, 37.36, 31.83, 26.55; ^{11}B (128 MHz, D_2O) δ 3.47.

PDADMA–[B(pyrazole)$_4$]. To 100 ml of an aqueous solution of PDADMA–OH and 6.73 g of H[B(pyrazole)$_4$] were used, PDADMA–[B(pyrazole)$_4$] was obtained as a dark grey solid. ^{1}H (400 MHz, D_2O) δ 7.47–7.61 (8H, s, –N–C**H**═, –N═C**H**–), 6.19 (4H, s, –CH═C**H**–), 3.68 (2H, s, C**H**$_2$–N$^+$), 2.99–3.11 (8H, m, –N–C**H**$_3$, C**H**$_2$–N$^+$), 2.56 (2H, s, –CH$_2$–C**H**–), 1.21–1.42 (4H, m, –C**H**$_2$–CH); ^{13}C (100 MHz, D_2O) δ 139.92, 135.69, 104.50, 70.26, 52.19, 38.18, 26.51; ^{11}B (128 MHz, D_2O) δ 2.67.

PDADMA–[B(triazole)$_4$]. To 100 ml of an aqueous solution of PDADMA–OH and 6.81 g of H[B(triazole)$_4$] were used, PDADMA–[B(triazole)$_4$] was obtained as a white solid. ^{1}H (400 MHz, D_2O) δ 8.25 (8H, s, –N═C**H**–), 3.81 (2H, s, C**H**$_2$–N$^+$), 3.12–3.23 (8H, m, –N–C**H**$_3$, C**H**$_2$–N$^+$), 2.68 (2H, s, –CH$_2$–C**H**–), 1.31–1.53 (4H, m, –CH$_2$–CH); ^{13}C (100 MHz, D_2O) δ 147.95, 70.25, 53.89, 38.15, 26.32; ^{11}B (128 MHz, D_2O) δ 3.67.

Conflicts of interest

There are no conflicts to declare.

Data availability

^{1}H, ^{13}C, and ^{11}B NMR spectra of H– and PDADMA–borates in D_2O, FT-IR and DSC data for PDADMA–borates, and electrochemical test results (CV, IV, and galvanostatic cycling) with Li-cathode coin cells containing polymer binders. See DOI: **https://doi.org/10.1039/D5LF00155B**.

The data supporting this article have been included as part of the SI.

Acknowledgements

The authors thank the SGIker of the University of the Basque Country (UPV/EHU) for access to XPS facilities, and acknowledge the European Regional Development Fund (ERDF) and the European Science Foundation (ESF) for support and funding. We thank Northern Ireland DfE for providing a PhD studentship to HA.

Notes and references

1 (*a*) Z. J. Baum, R. E. Bird, X. Yu and J. Ma, *ACS Energy Lett.*, 2022, **7**, 712–719; (*b*) J. Piątek, S. Afyon, T. M. Budnyak, S. Budnyk, M. H. Sipponen and A. Slabon, *Adv. Energy Mater.*, 2020, **11**, 2003456.

2 Q. He, J. Ning, H. Chen, Z. Jiang, J. Wang, D. Chen, C. Zhao, Z. Liu, I. F. Perepichka and H. Meng, *et al.*, *Chem. Soc. Rev.*, 2024, **53**, 7091–7157.

3 (*a*) X. Yu and A. Manthiram, *Adv. Energy Sustainability Res.*, 2021, **2**, 2000102; (*b*) Z. Cheng, H. Jiang, X. Zhang, F. Cheng, M. Wu and H. Zhang, *Adv. Funct. Mater.*, 2023, **33**, 2301109.

4 H. Chen, M. Ling, L. Hencz, H. Y. Ling, G. Li, Z. Lin, G. Liu and S. Zhang, *Chem. Rev.*, 2018, **118**, 8936–8982.

5 J. Asenbauer, T. Eisenmann, M. Kuenzel, A. Kazzazi, Z. Chen and D. Bresser, *Sustainable Energy Fuels*, 2020, **4**, 5387–5416.

6 (*a*) M. Wang, J. Hu, Y. Wang and Y.-T. Cheng, *J. Electrochem. Soc.*, 2019, **166**, A2151; (*b*) A. Cholewinski, P. Si, M. Uceda, M. Pope and B. Zhao, *Polymers*, 2021, **13**, 631.

7 (*a*) Y. Zhang, S. Lu, Z. Wang, V. Volkov, F. Lou and Z. Yu, *Renewable Sustainable Energy Rev.*, 2023, **183**, 113515; (*b*) M. Ryu, Y.-K. Hong, S.-Y. Lee and J. H. Park, *Nat. Commun.*, 2023, **14**, 1316.

8 (*a*) A. C. Rolandi, I. de Meatza, N. Casado, M. Forsyth, D. Mecerreyes and C. Pozo-Gonzalo, *RSC Sustainability*, 2024, **2**,

2125–2149; (*b*) A. C. Rolandi, C. Pozo-Gonzalo, I. de Meatza, N. Casado, M. Forsyth and D. Mecerreyes, *ACS Appl. Energy Mater.*, 2023, **6**, 8616–8625.

9 M. Zhu and Y. Yang, *Green Chem.*, 2024, **26**, 5022–5102.

10 (*a*) A. S. Shaplov, R. Marcilla and D. Mecerreyes, *Electrochim. Acta*, 2015, **175**, 18–34; (*b*) S.-Y. Zhang, Q. Zhuang, M. Zhang, H. Wang, Z. Gao, J.-K. Sun and J. Yuan, *Chem. Soc. Rev.*, 2020, **49**, 1726–1755.

11 (*a*) F. Lu, X. Gao, A. Wu, N. Sun, L. Shi and L. Zheng, *J. Phys. Chem. C*, 2017, **121**, 17756–17763; (*b*) W. Qian, J. Texter and F. Yan, *Chem. Soc. Rev.*, 2017, **46**, 1124–1159.

12 S. Chauque, F. Y. Oliva, O. R. Camara and R. M. Torresi, *J. Solid State Electrochem.*, 2018, **22**, 3589–3596.

13 S. Vauthier, M. Alvarez-Tirado, G. Guzman-Gonzalez, L. Tome, S. Cotte, L. Castro, A. Gueguen, D. Mecerreyes and N. Casado, *Mater. Today Chem.*, 2023, **27**, 101293.

14 (*a*) K. Grygiel, J.-S. Lee, K. Sakaushi, M. Antonietti and J. Yuan, *ACS Macro Lett.*, 2015, **4**, 1312–1316; (*b*) A. Vizintin, R. Guterman, J. Schmidt, M. Antonietti and R. Dominko, *Chem. Mater.*, 2018, **30**, 5444–5450; (*c*) J.-S. Lee, K. Sakaushi, M. Antonietti and J. Yuan, *RSC Adv.*, 2015, **5**, 85517–85522; (*d*) R. Del Olmo, G. Guzman-Gonzalez, I. O. Santos-Mendoza, D. Mecerreyes, M. Forsyth and N. Casado, *Batteries Supercaps*, 2023, **6**, e202200519.

15 A. C. Rolandi, C. Pozo-Gonzalo, I. De Meatza, N. Casado, D. Mecerreyes and M. Forsyth, *Adv. Energy Sustainability Res.*, 2023, **4**, 2300149.

16 H. Amir, M. Kar, L. A. O'Dell, M. Forsyth, M. Swadźba-Kwaśny and J. D. Holbrey, *J. Mater. Chem. A*, 2025, **13**, 18842–18850.

17 X. Sun, H. Hao, F. Zhao and Z. Liu, *Resour., Conserv. Recycl.*, 2017, **124**, 50–61.

18 (*a*) K. Dai, Y. Zheng and W. Wei, *Adv. Funct. Mater.*, 2021, **31**, 2008632; (*b*) B. Roy, P. Cherepanov, C. Nguyen, C. Forsyth, U. Pal, T. C. Mendes, P. Howlett, M. Forsyth, D. MacFarlane and M. Kar, *Adv. Energy Mater.*, 2021, **11**, 2101422; (*c*) H. Kang, M. Song, M. Yang and J.-W. Lee, *J. Power Sources*, 2021, **485**, 229286.

19 C. Chiappe, F. Signori, G. Valentini, L. Marchetti, C. S. Pomelli and F. Bellina, *J. Phys. Chem. B*, 2010, **114**, 5082–5088.

20 S. Chao and C. E. Moore, *Anal. Chim. Acta*, 1978, **100**, 457–467.

21 (*a*) C. C. Zhang, X. Gao and B. Yilmaz, *Catalysts*, 2020, **10**, 1327; (*b*) Y. Zhou, R. Sun, Z. Zhang, W. Fan, D. Zhou and C. Sheng, *Results Phys.*, 2017, **7**, 705–708.

22 (*a*) Q. Zhang, Z. Sha, X. Cui, S. Qiu, C. He, J. Zhang, X. Wang and Y. Yang, *Nanotechnol. Rev.*, 2020, **9**, 1350–1358; (*b*) M. Ndour, J.-P. Bonnet, S. Cavalaglio, T. Lombard, M. Courty, L. Aymard, C. Przybylski and V. Bonnet, *Mater. Adv.*, 2022, **3**, 8522–8533.

23 J. Entwistle, R. Ge, K. Pardikar, R. Smith and D. Cumming, *Renewable Sustainable Energy Rev.*, 2022, **166**, 112624.

24 M. Ling, J. Qiu, S. Li, C. Yan, M. J. Kiefel, G. Liu and S. Zhang, *Nano Lett.*, 2015, **15**, 4440–4447.

25 S. Rajendran, H. Liu, S. E. Trask, B. Key, A. N. Jansen and M.-T. Rodrigues, *J. Power Sources*, 2023, **583**, 233584.

26 A. C. Rolandi, N. Casado, A. Somers, I. de Meatza, D. Mecerreyes, C. Pozo-Gonzalo, P. C. Howlett, R. Kerr and M. Forsyth, *J. Power Sources Adv.*, 2024, **30**, 100161.

27 B. Chen, Z. Zhang, M. Xiao, S. Wang, S. Huang, D. Han and Y. Meng, *ChemElectroChem*, 2024, e202300651.

28 Y. Lakhdar, Y. Chen, H. Geary, M. E. Houck, A. S. Groombridge, P. R. Slater and E. Kendrick, *J. Power Sources*, 2023, **588**, 233710.

29 J. Olmos, I. Gandiaga, A. Saez-de Ibarra, X. Larrea, T. Nieva and I. Aizpuru, *J. Energy Storage*, 2021, **40**, 102765.

30 M. W. Bo, A. Arulrajah, S. Horpibulsuk, A. Chinkulkijniwat and M. Leong, *Soils Found.*, 2016, **56**, 129–137.

31 Z. W. Lebens-Higgins, S. Sallis, N. V. Faenza, F. Badway, N. Pereira, D. M. Halat, M. Wahila, C. Schlueter, T.-L. Lee and W. Yang, *et al.*, *Chem. Mater.*, 2018, **30**, 958–969.

32 K. Liu, Q. Zhang, S. Dai, W. Li, X. Liu, F. Ding and J. Zhang, *ACS Appl. Mater. Interfaces*, 2018, **10**, 34153–34162.

33 B. K. Mutuma, B. J. Matsoso, D. Momodu, K. O. Oyedotun, N. J. Coville and N. Manyala, *Nanomaterials*, 2019, **9**, 446.

34 Y. Dong, B. T. Young, Y. Zhang, T. Yoon, D. R. Heskett, Y. Hu and B. L. Lucht, *ACS Appl. Mater. Interfaces*, 2017, **9**, 20467–20475.

35 Y. Xiao, J.-R. Zhang, S.-Y. Wang and W. Hua, *Precis. Chem.*, 2024, **2**, 239–244.

36 M.-P. Tran, P. Gonzalez-Aguirre, C. Beitia, J. Lundgren, S.-I. Moon and H. Fontaine, *Microelectron. Eng.*, 2019, **207**, 1–6.